Synthesis of Two Classes of Acoustic Surface-Wave Filter Tap Weights

GEORGE L. MATTHAEI, FELLOW, IEEE, DAVID Y. WONG, STUDENT MEMBER, IEEE, AND BRIAN P. O'SHAUGHNESSY, STUDENT MEMBER, IEEE

Abstract—**Techniques are presented for the synthesis of interdigital acoustic surface-wave filter tap weights so as to give transfer functions having a Chebyshev stopband attenuation characteristic with a specified minimum attenuation, along with a single-peaked or a Chebyshev double-peaked passband characteristic. The techniques first give the gain zero locations, and as a result are very flexible. Linear phase or minimum or maximum phase-shift characteristics are obtainable. The transfer function can be factored into two sets of zeros which can be realized as two separate apodized transducers which, when operated with a multistrip coupler, will give the desired overall transfer function. Also, it is shown that the class of designs having a double-peaked passband can be realized in the form of an unapodized phase-reversal transducer (PRT) in cascade with a second transducer having very smooth apodization and no phase reversals. The fact that such designs have such smooth apodization with relatively few small taps can help in obtaining precision performance.**

I. INTRODUCTION

IN this paper, methods for the determination of finger tap weights for the two transducers required in an interdigital acoustic surface-wave filter are treated. Various tap-weight design procedures are presented that yield either of two general classes of Chebyshev filter transfer functions.

Each tap, in the discussion to follow, is realized by the gap between two fingers of an interdigital transducer, and the taps are equally spaced. The magnitude of a tap weight is determined by the active overlap length of the two adjacent fingers, and the sign of the weight is determined by the relative polarity of the electric field in the gap. Since the taps correspond to the finger gaps, it takes $n + 1$ fingers to realize n taps.

It is assumed that the transducer electric ports are lightly loaded so that electrical interaction effects can be neglected. In this case it can be seen that the tap weights (put in functional form as a sequence of impulses) approximate the impulse response of the transducer. Then the frequency response of a transducer will, of course, be related to the tap weights by the Fourier transform. In the designs under consideration the overall transfer function is the product of the transforms for the two transducers.

Manuscript received April 7, 1975; revised July 17, 1975. This work was supported by the National Science Foundation under Grants GK-35478X and ENG72-04059 A02.

The authors are with the Department of Electrical Engineering and Computer Science, University of California, Santa Barbara, CA 93106.

Since the impulse responses of the filters under discussion consist of equally spaced weighted impulses, Fourier analysis shows that the frequency response must be periodic. It further can be shown that the transfer function corresponding to such impulse responses will have only zeros on the finite plane, all of the poles of the function being combined in an essential singularity at infinity. This is a severe restriction on the transfer function since the poles are the natural frequencies of vibration of the circuit, and one would ordinarily place them adjacent to the passbands of the filter. If it were not for this limitation on the poles, it would take many fewer taps to realize a desired transfer function.

In the discussion to follow, filters with two types of transfer functions designated type 0 and type 2 will be discussed. Both have "equal-ripple" attenuation in their stopbands. Type 2 differs from type 0 in that it is capable of a much flatter passband, but at a price of appreciably more taps. The type number indicates the number of zeros in the transfer function *off* of the $j\omega$ axis *per period* of the transfer function. Thus the type 0 design has all of its zeros on the $j\omega$ axis while the type 2 design has two zeros per period off the $j\omega$ axis as well as zeros on the $j\omega$ axis.

II. TYPE 0 DESIGNS

As indicated previously, the type 0 designs have all their transfer function zeros on the $j\omega$ axis and all of the poles at infinity. Fig. 1 shows a sample response for such a design. Note that the attenuation level is equal ripple in the stopband and has a minimum attenuation designated by ATN. The response has arithmetic symmetry about the frequency ω_0, and the response is periodic, one period

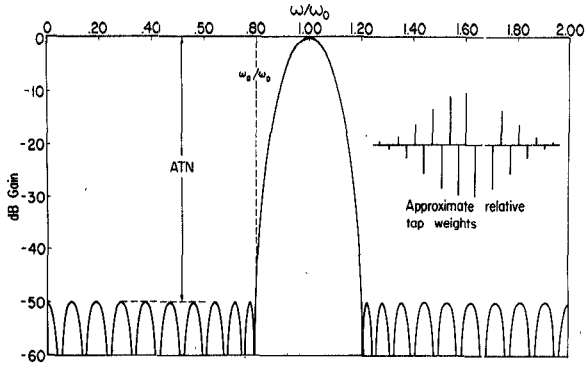

Fig. 1. Response for a type 0 design with $M = 20$.

of the response being shown in Fig. 1. The width of the stopband is established by the parameter ω_a/ω_0. Distinctive features of this transfer function are its equal-ripple stopband characteristic and the fact that the passband is necessarily rounded at the top.

The tap weights for designs of the sort in Fig. 1 could be obtained by adaptation of Dolph–Chebyshev antenna design procedures [1]. However, herein a different approach was used which involved two conformal mappings and, at least for the purposes herein, this approach appears to be simpler than the methods commonly used for antennas.

Let us now consider the design of tap weights so as to obtain a transfer function such as that in Fig. 1. Let M be the number of zeros per period for the filter response, where herein for a type 0 design M is required to be an *even number*. In Fig. 1, $M = 20$ since there are 20 points at which the attenuation is infinite within the frequency response period. For given values of M and ω_a/ω_0 the minimum stopband attenuation is given by

$$\text{ATN} = 20 \log_{10} \cosh \left[\frac{M}{2} \cosh^{-1} \left(\frac{2 - \sin^2 (\pi\omega_a/2\omega_0)}{\sin^2 (\pi\omega_a/2\omega_0)} \right) \right] \text{dB}. \tag{1}$$

The location of the zeros of the transfer function which lie between $\omega = 0$ and $\omega = \omega_0$ are given by

$$\left. \frac{\omega_k}{\omega_0} \right|_{k=1 \text{ to } M/2} = \frac{2}{\pi} \sin^{-1} \left[\sin \left(\frac{\pi}{2} \frac{\omega_a}{\omega_0} \right) \cdot \left(\frac{1 - \cos [(2k-1)\pi/M]}{2} \right)^{1/2} \right]. \tag{2}$$

Having determined these zeros, the remaining zeros are determined by symmetry and the periodic nature of the transfer function. The derivations of (1) and (2) are discussed in Appendix A.

The overall transfer function can be specified starting with a Chebyshev polynomial and applying the mappings discussed in Appendix A. However, for our present purposes it will be more convenient to specify the transfer function in the form

$$G_A(\omega) = C_A \prod_{k=1}^{M/2} \left[\sin \left[\frac{(\omega - \omega_k)\pi}{2\omega_0} \right] \sin \left[\frac{(\omega + \omega_k)\pi}{2\omega_0} \right] \right]. \tag{3}$$

This function constructs all of the required zeros for the transfer function by use of factors for zeros at ω_k and $-\omega_k$, and then generating the infinite array of zeros required for periodicity by introducing sine functions. The parameter C_A in front is an arbitrary constant which can be conveniently chosen to make $G_A(\omega_0) = 1$.

Equation (3) is a form for the transfer function which is particularly convenient for the purpose of taking the inverse Fourier transform. If we take the inverse Fourier transform of the pair of sine functions shown in (3), we obtain

$$T_k(t) = \tfrac{1}{2} \cos (\pi\omega_k/\omega_0)\delta(t) - \tfrac{1}{4}[\delta(t - \pi/\omega_0) + \delta(t + \pi/\omega_0)]. \tag{4}$$

Since (3) consists of a product of pairs of sine functions, the inverse Fourier transform for the overall transfer function can be obtained by convolution of the transforms of the various sine-function pairs. Thus the impulse response for the filter is obtained by the multiple convolution

$$h_A(t) = C_A T_1(t) * T_2(t) * \cdots * T_{M/2}(t) \tag{5}$$

where the $T_k(t)$ are as defined in (4). Since the $T_k(t)$ consist only of delta functions, the convolution in (5) is very easy to accomplish [2] and results in a sequence of weighted delta functions (i.e., the tap weights).

We have found that, at least for some cases when M is large (say, 70 or more), the accuracy of the multiple convolutions in (5) may degenerate. In such cases the accuracy is greatly improved by first computing the frequency response by use of (3) or (A4) of Appendix A. Then the taps are obtained by use of a discrete Fourier transform routine such as that in the IBM 360 Scientific Subroutine Package. Note that in this application the fast Fourier transform usually is not desirable since it is specifically limited to cases having 2^N samples.

In the upper right of Fig. 1 is shown the approximate relative tap weights obtained by (5) for this example. Note that for $M = 20$ zeros per period the design process results in $M + 1 = 21$ taps, which calls for $M + 2 = 22$ fingers in the transducer. Also note that the tap weights are more or less triangular in distribution and hence should be reasonably easy to realize. As discussed in Section VI, the second transducer to be used in conjunction with one apodized as in Fig. 1 can usually be a uniform transducer with a sizable number of fingers.

III. TYPE 2 DESIGNS

Where type 0 designs are usable, they are very desirable because of their simplicity of calculation, because of their relatively smooth apodization with no phase reversals, and because they require relatively few taps. However, type 0 designs necessarily have rounded passbands, and if the desired signal is of wide bandwidth, this might not be acceptable. Since we are constrained to keep all of the poles of the transfer function at infinity, the only way that the passband can be flattened is by introduction of zeros off the $j\omega$ axis in the vicinity of the passband. This is illustrated in the complex frequency plane (i.e., $p = \sigma + j\omega$ plane) plot in Fig. 2(b). In this plot the zeros are sketched for a transfer function having $M = 6$ $j\omega$-axis zeros per period. (Herein M will always be the number of zeros per period on the $j\omega$ axis only, and for type 2 designs M can be odd or even.) The pairs of off-axis zeros near the passbands have the effect of putting a dip in the center of the passband, as is indicated in the $M = 29$ example plotted in Fig. 3. The term "type 2 design" will herein refer to designs having two zeros per period off of the $j\omega$ axis. It would have been possible to have achieved

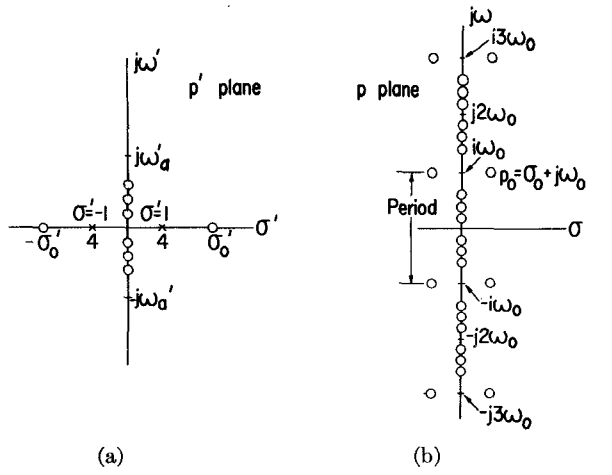

Fig. 2. (a) High-pass-prototype transfer function. (b) Bandpass type 2 transfer function.

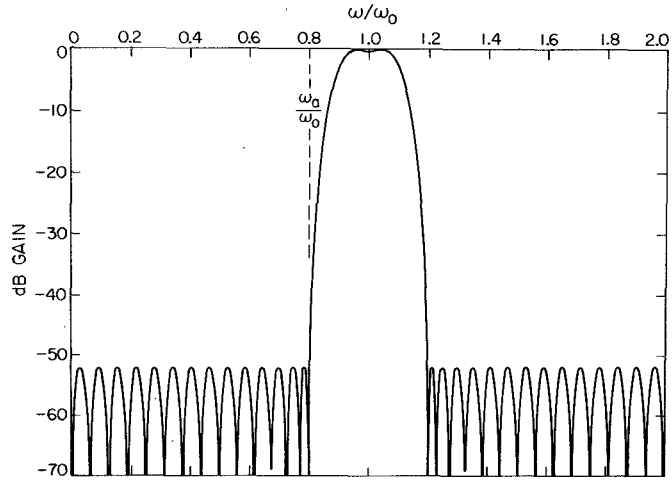

Fig. 3. Frequency response for a type 2 design with $M = 29$.

the desired effect in the response magnitude by use of only one zero per period off the $j\omega$ axis, but this would eliminate the possibility of having linear phase. The arrangement of zeros in Fig. 2(b) has quadrantal symmetry which guarantees that the $j\omega$ axis will be a contour of constant phase except for a jump of π at each zero on the $j\omega$ axis.[1] If, say, only the zeros in the left half-plane were included, it would be possible to flatten the magnitude of the response in the passband, but the $j\omega$ axis would no longer be a contour of constant phase.

Our design procedure for obtaining tap weights for transfer functions like that in Fig. 3 is to first obtain a high-pass prototype design using design equations obtained with the aid of an electrostatic potential analogy [3], [4] (see Appendix B). Miller [5] used similar methods to treat some related (but different) transfer functions. Fig. 2(a) shows a pole and zero plot in a p' plane for a high-pass prototype transfer function corresponding to the desired p-plane function in Fig. 2(b). The desired bandpass function and the high-pass prototype will both have the same stopband attenuation and passband ripple. The prototype can be mapped to the desired function by use of the conformal mapping

$$p' = \tanh\left(\frac{\pi p}{2\omega_0}\right). \tag{6}$$

Note that the transfer function in the p' plane in Fig. 2(a) has fourth-order poles at $p' = \sigma' = \pm 1$, which map to the point at infinity in the p plane. The $j\omega'$-axis zeros in the p' plane map to periodic $j\omega$-axis zeros in the p plane, while the zeros at $\pm\sigma_0'$ in the p' plane map to periodic zeros off the $j\omega$ axis in the p plane. Points on the imaginary axis in the two planes are related by

$$\omega' = \tan\left(\frac{\pi\omega}{2\omega_0}\right). \tag{7}$$

Let ω_a be the lower frequency stopband edge indicated by the dashed line in Fig. 3. The corresponding high-pass prototype stopband edge is given by

$$\omega_a' = \tan\left(\frac{\pi\omega_a}{2\omega_0}\right) \tag{8}$$

in the p' plane.

The attenuation characteristic of the high-pass prototype can be obtained from

$$\mathrm{dB}' = 10\log_{10}\left[\frac{U^2}{4} + \frac{1}{4U^2} \pm \tfrac{1}{2}\right] \tag{9}$$

where for $\omega' > \omega_a'$

$$U = \left[\frac{[(\omega'/\omega_a')^2 - 1]^{1/2} + m_0(\omega'/\omega_a')}{[(\omega'/\omega_a')^2 - 1]^{1/2} - m_0(\omega'/\omega_a')}\right]^{(M+2)/2} \cdot \left[\frac{[(\omega'/\omega_a')^2 - 1]^{1/2} - m_1(\omega'/\omega_a')}{[(\omega'/\omega_a')^2 - 1]^{1/2} + m_1(\omega'/\omega_a')}\right] \tag{10}$$

and where

$$m_0 = (1 + \omega_a'^2)^{1/2}$$

$$m_1 = \left[1 + \left(\frac{\omega_a'}{\sigma_0'}\right)^2\right]^{1/2}. \tag{11}$$

In (9), the upper sign is for M even and the lower sign is for M odd. In (11), σ_0' is the location of the right-hand σ' axis zero in Fig. 2(a). Fig. 4 shows a sketch of a typical high-pass prototype attenuation characteristic for the case of $M = 6$. Notice that the zero-dB reference level has been taken at the crest of the stopband ripples. The stopband attenuation level ATN as defined in Fig. 4 can be calculated by use of (9) with $\omega' \to \infty$ so

$$U = U_\infty = \left(\frac{1 + m_0}{1 - m_0}\right)^{(M+2)/2}\left(\frac{1 - m_1}{1 + m_1}\right). \tag{12}$$

For a given design usually ω_a' will be known from (8). In order to obtain a design with a desired value of ATN

[1] The reference ports for the transfer functions derived herein are at the center of the transducer. Moving the acoustic reference ports to the ends of the transducers adds linear phase.

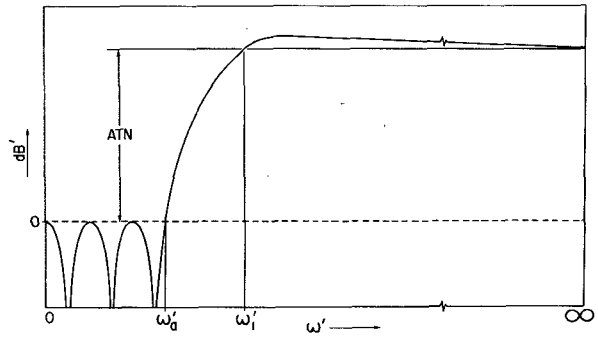

Fig. 4. Approximate decibel frequency response for the transfer function in Fig. 2(a).

and with a given passband Chebyshev ripple, it is necessary to search for appropriate values of M and σ_0'. We have done this conveniently by programming (9)–(11). For a given ω_a' and trial value of M the program searches for a value of σ_0' that will achieve the desired passband ripple. A good starting value for σ_0' to use can be obtained from

$$D = \left[\frac{(M+2)}{2}\left(\frac{m_0}{m_0^2-1}\right)\right]^{-1} \tag{13}$$

$$m_1 = \frac{D + (D^2+4)^{1/2}}{2} \tag{14}$$

$$(\sigma_0')_{\text{flat}} = \frac{\omega_a'}{(m_1^2-1)^{1/2}}. \tag{15}$$

This value of σ_0' will give a maximally flat passband, and in order to obtain a Chebyshev ripple in the passband, one should use a value of σ_0' greater than $(\sigma_0')_{\text{flat}}$. If the value of ATN obtained for the given passband ripple is too small, then a larger value of M must be used.

After appropriate design values for M and σ_0' have been obtained, the $j\omega'$-axis zero locations ω_k' are obtained by solving

$$(M+2)\tan^{-1}\left[\frac{m_0\omega_k'/\omega_a'}{[1-(\omega_k'/\omega_a')^2]^{1/2}}\right] - 2\tan^{-1}\left[\frac{m_1\omega_k'/\omega_a'}{[1-(\omega_k'/\omega_a')^2]^{1/2}}\right]$$
$$= (2k-1)(\pi/2)\,|_{k=1 \text{ to } J}, \quad \text{if } M = \text{even}$$
$$= k\pi\,|_{k=0 \text{ to } J}, \quad \text{if } M = \text{odd} \tag{16}$$

for the ω_k'. In (16)

$$J = M/2 \quad \text{if } M = \text{even}$$
$$J = (M-1)/2 \quad \text{if } M = \text{odd}. \tag{17}$$

Having the ω_k' in the p' plane, the corresponding zeros for the primary period of the function in the p plane are obtained by

$$\omega_k = (2\omega_0/\pi)\tan^{-1}\omega_k'\,\Big|_{\substack{k=1 \text{ to } J \text{ for } M \text{ even} \\ k=0 \text{ to } J \text{ for } M \text{ odd}.}} \tag{18}$$

The zeros at $p = \pm\sigma_0 + j\omega_0$ indicated in Fig. 2(b) are located with the aid of the equation

$$\sigma_0 = (2\omega_0/\pi)\coth^{-1}\sigma_0'. \tag{19}$$

The transfer function for type 2 designs is seen to be

$$G_B(\omega) = C_B[\tfrac{1}{2}\cosh(\sigma_0\pi/\omega_0) - \tfrac{1}{2}\cos((\omega-\omega_0)\pi/\omega_0)][\sin(\omega\pi/2\omega_0)] \cdot \prod_{k=1}^{J}\sin[(\omega-\omega_k)\pi/2\omega_0]\sin[(\omega+\omega_k)\pi/2\omega_0]. \tag{20}$$

Note that (20) has two factors not included in (3) for type 0 designs. The first square-bracketed factor introduces the complex zeros at $p = \pm\,|\,\sigma_0\,| + j\omega_0$ and at periodic repetitions of these points. The second square-bracketed factor gives zeros at $\omega = 0, 2\omega_0$, etc., and *should only be included when M is odd.* The multiplier C_B is a constant which can be adjusted to fix the minimum loss ratio.

The inverse Fourier transforms of the first and second square-bracketed terms in (20) are, respectively,

$$T_\sigma(t) = \cosh(\sigma_0\pi/\omega_0)[\delta(t)/2] + \tfrac{1}{4}[\delta(t-\pi/\omega_0) + \delta(t+\pi/\omega_0)] \tag{21}$$

and

$$T_0(t) = \tfrac{1}{2}[\delta(t-\pi/2\omega_0) - \delta(t+\pi/2\omega_0)]. \tag{22}$$

The transforms of the remaining factors in (20) giving $j\omega$-axis zeros are obtained by (4). Again the impulse response can be obtained from the convolution [2] of these various transforms as indicated by

$$h_b(t) = C_B T_\sigma(t) * T_0(t) * T_1(t) * \cdots * T_J(t) \tag{23}$$

or by computing $G_B(\omega)$ and using the discrete Fourier transform. For a design having M $j\omega$-axis zeros per period of response, there will be $M+3$ tap weights required and $M+4$ transducer fingers.

The solid line in Fig. 3 shows the computed response for a design having $\omega_a/\omega_0 = 0.8$ and ATN about 52 dB, similar to the design in Fig. 1 but with 0.2-dB Chebyshev ripple in the passband. This design has $M = 29$, $\sigma_0' = 7.5359$, and $\sigma_0/\omega_0 = 0.084979$. The presence of complex zeros near the passband in type 2 designs tends to weaken the passband, and, as a result, more stopband zeros are required in order to achieve a desired value of ATN. Thus the type 2 design required 32 taps as compared to only 21 for the analogous type 0 design in Fig. 1. The resulting tap weights are shown in Fig. 5(a). Note that they are symmetrical and have a phase reversal toward the outer ends of the tap sequence.

IV. SOME DESIGN VARIATIONS

Filter design from the pole and zero viewpoint has an advantage of flexibility. For example, if we wish we can obtain a design for the transfer function in Fig. 2(b) having the same magnitude for frequencies $j\omega$ but with

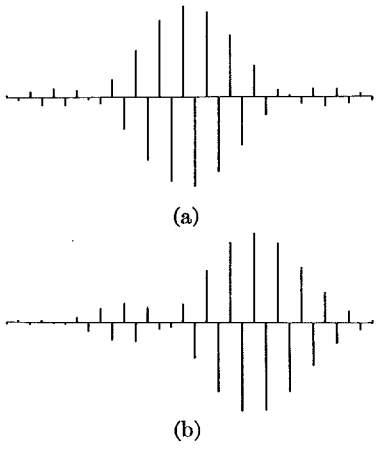

Fig. 5. Tap weights for two type 2 designs with $M = 29$. (a) Case of linear phase. (b) Design giving minimum phase when communicating with a wide-band transducer on the right.

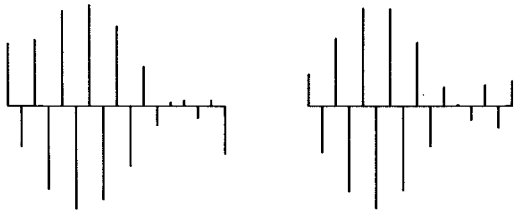

Fig. 6. The design in Fig. 5(a) factored into two sets of transducer tap weights. (A multistrip coupler would be required between these two transducers.)

the left-half-plane zeros moved over to the right half-plane to yield double zeros there. A possible disadvantage of such a design is that it would no longer have linear phase since the zero pattern would no longer have quadrantal symmetry. However, as a matter of interest, such a design was worked out with the solid-curve magnitude characteristic in Fig. 3 and with double right-half-plane zeros. The resulting tap weights are shown in Fig. 5(b). If this transducer transmits to a wide-band transducer placed on the left, the overall transfer function will have double zeros in the right half-plane; whereas if this configuration transmits to a wide-band transducer placed on the right, the overall transfer function will have double zeros in the left half-plane. Fig. 5(a) and (b) also illustrates the point that symmetry in the transducer configuration goes along with linear phase.

Another variation of the solid-curve design in Fig. 3 was obtained by partitioning the overall transfer function into two factors by separating alternate $j\omega$-axis zeros and assigning each factor one of the off-$j\omega$-axis zeros. Then one factor was used to realize one transducer while the other factor was used to realize the other transducer. When used in conjunction with an intervening multistrip coupler [6], [7], the overall transfer function will, in theory, be the product of the transfer functions for the two individual apodized transducers. Fig. 6 shows the tap weights for the two transducers. It is of interest to note that in the case of a previous $M = 28$ design (which had no zero at $\omega = 0$), when the transfer function was factored into two parts, one of the resulting two transducers had a sequence of positive taps [12]. Such a sequence would not be acceptable for use in an acoustic surface-wave filter. The use of an $M = 29$ design, which has a zero at $\omega = 0$ and adjacent zeros relatively close to $\omega = 0$, avoids this problem since the frequency response for both factors is either zero or small at $\omega = 0$. (A sequence of taps with the same sign can result from a sizeable frequency response at dc.)

V. INCORPORATION OF A PHASE-REVERSAL TRANSDUCER

In the left of Fig. 7(b) is shown a tap-weight configuration such as can be realized using the unapodized phase-reversal type of transducer (PRT) introduced by Bristol [8]. It can be shown that this type of transducer realizes a set of zeros off of the $j\omega$ axis such as those off-axis zeros shown in Fig. 2(b), along with additional zeros on the $j\omega$ axis. Thus a transfer function such as that in Fig. 2(b) can be realized approximately by use of an unapodized PRT in cascade with an apodized transducer which has no phase reversals. Apodization of the second transducer is needed in order to realize the $j\omega$-axis zeros not already satisfactorily realized by the PRT. Since only one of the transducers is apodized, the overall transfer function is simply the product of the transfer functions for the two individual transducers [10].

Fig. 7 illustrates these principles. Fig. 7(a) shows a 75-tap type-2 design obtained by the methods of Section III. By itself it gives a frequency response like that in Fig. 8, except that it has very accurately controlled equal ripples in its stopbands with the ripple crests along the horizontal dashed line in the figure. This design has zeros off the $j\omega$ axis as suggested in Fig. 2(b) with $|\sigma_0/\omega_0| = 0.036628$. Such zeros can be realized approximately using the unapodized PRT taps on the left in Fig. 7(b). The PRT also introduces other zeros on the $j\omega$ axis, some of

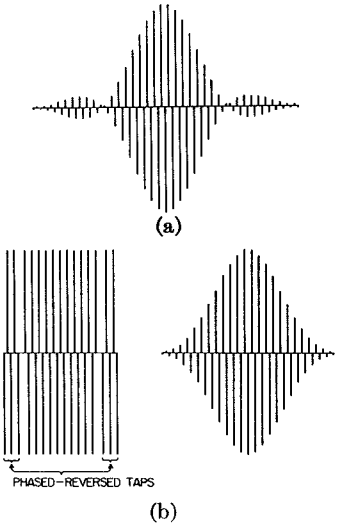

Fig. 7. (a) An $M = 72$ type 2 design. (b) Two transducer tap sequences which when operated in cascade give nearly the same response as for the tap weights at (a).

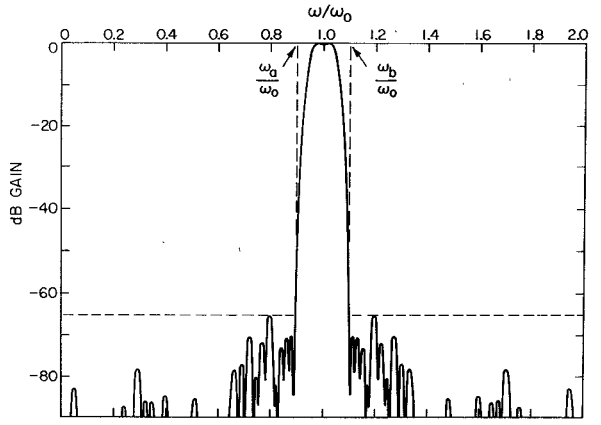

Fig. 8. Frequency response for the tap weights in Fig. 7(b) in cascade. [The horizontal dashed line indicates the equal-ripple attenuation level for the design in Fig. 7(a).]

which are quite close to the $j\omega$-axis zero locations needed for the desired transfer function given in (20). Thus the zeros not already realized by the PRT are grouped together and realized by a second transducer (which is type 0 since it has only $j\omega$-axis zeros). For this example the apodized transducer design came out as shown at the right in Fig. 7(b). Note that the apodization is very smooth with relatively few small taps, a situation which should help in the practical realization of the taps. The resultant response is as shown in Fig. 8 where the stopband attenuation for the transducers in Fig. 7(b) in cascade everywhere equals or exceeds that of the design in Fig. 7(a) (indicated by the horizontal dashed line), while the passband characteristics are very nearly the same as for the design in Fig. 7(a).

The design of a PRT with taps such as those in Fig. 7(b) can be worked out as follows. For frequencies $p = j\omega$ the transfer function for a PRT is given by[2]

$$G_{\mathrm{PR}}(\omega) = \frac{\sin[N_c u] + \sin[(N_c+2)u] - \sin[Nu]}{\sin u} \tag{24}$$

where

$$u = \frac{\pi}{2}\left(\frac{\omega - \omega_0}{\omega_0}\right).$$

In (24) N_c is the number of taps in the center section of the transducer indicated in Fig. 7(b), and N is the total number of tap *positions* in the transducer including the positions of the zero taps at the phase reversals. Thus the design in Fig. 7(b) has 31 nonzero taps, plus 2 zero taps, giving $N = 33$.

One restriction on the design of the PRT is that it must not produce any $j\omega$-axis zeros in the passband region between ω_a and ω_b indicated in Fig. 8. Investigation shows that the location of the $j\omega$-axis zeros closest to ω_0, the passband center, is in typical cases controlled predominantly by N_c. As a rough estimate the largest value of N_c that can be used is approximately

$$(N_c)_{\max} \approx \frac{2}{1 - \omega_a/\omega_0}. \tag{25}$$

At the complex frequencies $p = \pm\sigma_0 + j\omega_0$ (and their periodic repetitions) where zeros of G_{PR} are desired, (24) becomes

$$G_{\mathrm{PR}}(\pm\sigma_0 + j\omega_0) = \frac{\sinh[N_c w] + \sinh[(N_c+2)w] - \sinh[Nw]}{\sinh w} \tag{26}$$

where

$$w = \frac{\pi\sigma_0}{2\omega_0}.$$

Our only degrees of freedom for achieving the desired zeros are in our choices of N_c and N. Thus it will usually not be possible to realize the desired value of σ_0 exactly. However, in the several examples we have tried it was possible to achieve a value for σ_0 satisfactorily close to the desired value. (If desired, more degrees of freedom can be introduced by allowing for the possibility of more than one zero tap at the phase reversals.) For an exact design (26) would be equal to zero. Thus the desired approximate design is obtained by searching for the values of N_c and N which make (26) as small as possible. Our procedure was to prepare a computer program to evaluate (26) and find the minimum value of G_{PR} for trial values of N, while at first N_c is held fixed at $(N_c)_{\max}$. Next, N_c is reduced in size by one, and the minimum value versus N is again sought. This routine quite quickly arrived at values of N_c and N giving a good approximate solution. It is conceivable that in some cases one might want to explore larger values of N_c than indicated by (25), and somewhat larger values might be acceptable in some cases since (25) is only approximate. Solutions using larger values of N_c should be checked using (24) in order to be sure there are no zeros between ω_a and ω_b.

After values of N_c and N for the PRT are determined, the $j\omega$-axis zeros introduced by the PRT can be determined from (24). These zeros could be simply added to the ones in (20), but it is found to be desirable to thin the zeros out some or the passband will be narrowed. This is particularly true for excess zeros immediately adjacent to the passband. Excess $j\omega$-axis zeros well away from the passband increase attenuation in that region but have little other effect. Many of the zeros from the PRT will be quite close to locations called for by the transfer function, so the apodized transducer need supply only part of the $j\omega$-axis zeros. It is not difficult to make a reasonably good selection of zeros but it is good to check the overall transfer function versus frequency after a selection has been made. This is readily done by taking the product of (24) for the PRT and (3) for the apodized transducer.

It is probable that this technique of realizing transfer functions using an unapodized transducer with phase reversals along with an apodized transducer can be extended to treat cases with more than two ripples in the passband. However, further mathematical derivations will be needed for such cases.

[2] Bristol [8] gave (24) herein with (using our notation) u rather than $\sin u$ in the denominator; that is usually a satisfactory approximation. However, (24) gives the exact response for taps such as those in Fig. 7(b) [11].

VI. PHYSICAL REALIZATION OF THE TAPS

This paper is addressed primarily to the problem of determining appropriate tap weights for certain types of bandpass filters. However, there are additional considerations involved in the practical realization of these taps, and it appears appropriate to make some brief mention of them.

Since in surface-wave filters of the types under consideration it is necessary to go from electrical to mechanical energy and back again, two transducers are always required. For a design like that in Fig. 1 the second transducer can be one with a reasonably large number of fingers having uniform length and with no reversals in the finger sequence. This second transducer would increase the stopband attenuation and narrow the passband somewhat, but these effects would presumably be acceptable if a rounded passband as in Fig. 1 were adequate for the application at hand. Designs such as those in Fig. 5(a) and (b) and in Fig. 7(a), which are intended to yield a relatively square passband region, would require the use of a wide-band output transducer having only a few fingers if the passband is not to be distorted. This would typically result in an unnecessarily large minimum loss for the filter. In addition, the relatively large number of small taps (i.e., small finger overlaps) in these designs may lead to performance errors due to diffraction and also due to the fringing fields at the ends of the fingers being a significant percent of the desired small effective overlap. These sources of error are minimized in the design in Fig. 1 which has very smooth apodization with relatively few small taps and no phase reversals.

If the overall transfer function is to be realized using two apodized transducers as in Fig. 6, it is necessary to use a multistrip coupler between the two transducers [7], or else the response will be greatly distorted [10]. This approach can give good results and the multistrip coupler has an added advantage of helping to reduce bulk-wave responses [7]. However, the inclusion of a multistrip coupler also has disadvantages of introducing more loss, requiring a more complex photomask, and requiring a larger substrate since the device pattern must be twice as wide. In addition, if the overall transfer function is factored to realize two transducers as in Fig. 6, or if two transducers as in Fig. 7(a) are used, the transducers will again involve a sizable number of relatively small taps with phase reversals.

Though the various approaches previously outlined can give satisfactory results if properly implemented, the use of designs such as that in Fig. 7(b) appears to us to provide a potentially attractive means for implementing precision designs. The apodized transducer on the right is of type 0. Thus it has no phase reversals, and has a smooth apodization with relatively few small taps. These factors should help to improve the accuracy of tap realization. Also since the PRT on the left is unapodized, no multistrip coupler is required. However, our initial experiments with PRT's indicate that some additional work on the design of PRT's is desirable. This is because if the PRT is composed of electrodes with uniform widths and gaps throughout, the effective tap strengths at the ends of the transducer and in the vicinities of the phase reversals are somewhat different than those in the rest of the transducer due to the different patterns of the interelectrode fringing electric fields in these regions. This results in a somewhat oversized passband ripple with slightly unequal minimum attenuation points, and also causes some small errors in the $j\omega$-axis zero locations. We believe that at least in or near the fundamental passband the frequency response errors due to these transition-region fringing field patterns can be compensated by proper altering of the finger widths and gaps in the vicinities of the ends of the transducer and in the vicinity of the phase reversals. We propose to investigate this matter in the future.[3] Such refinement of the PRT design should help to achieve unusually good design accuracy for designs as in Fig. 7(b).

APPENDIX A

DERIVATION OF EQUATIONS FOR THE TYPE 0 CASE

The equations for the type 0 case are readily derived starting from a Chebyshev polynomial

$$T_n(\omega'') = \cos(n \cos^{-1} \omega'') \qquad \text{(A1)}$$

and then applying conformal mappings. Fig. 9(a) shows a sketch of a Chebyshev polynomial versus ω'' for the case of $n = 4$. The polynomial in (A1) is then mapped to

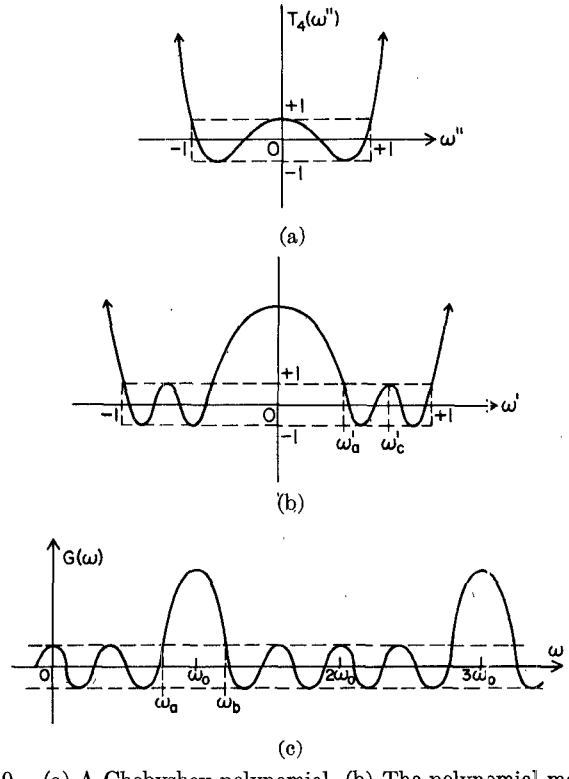

Fig. 9. (a) A Chebyshev polynomial. (b) The polynomial mapped by (A2). (c) The previous result mapped again by (A3).

[3] References [13] and [14] analyze the fringing effects about structures with fixed finger widths and periods, where the structure may have phase reversals and/or missing fingers. The investigation proposed differs in that, while most of the finger widths and periods remain fixed, some of the finger widths and positions would be modified in order to more accurately realize the given taps.

a new frequency variable ω' by use of the mapping

$$\omega'' = \frac{\omega'^2 - \omega_c'^2}{A} \tag{A2}$$

where

$$A = \frac{1 - \omega_a'^2}{2}$$

and

$$\omega_c' = \left(\frac{1 + \omega_a'^2}{2}\right)^{1/2}.$$

Fig. 9(b) illustrates the effect of this mapping on the polynomial in Fig. 9(a). Here ω_a' is an equal-ripple band-edge frequency which is arbitrary within the limits $0 < \omega_a' < 1$. The frequency ω_c' is the mapping of the original zero frequency $\omega'' = 0$.

The function in Fig. 9(b) has some of the desired form but is not yet the desired function since it is not periodic, and since it increases monotonically for $|\omega'| > 1$. To get the desired result we introduce the additional mapping

$$\omega' = -\cos\left(\frac{\pi\omega}{2\omega_0}\right) \tag{A3}$$

which converts the function in Fig. 9(b) to the form in Fig. 9(c). Here ω_0 is the passband-center frequency, and the mapping has the effect of mapping the region from $\omega' = -1$ to $\omega' = +1$ in Fig. 9(b) to the region $\omega = 0$ to $\omega = 2\omega_0$ in Fig. 9(c), and also to periodic repetitions of this region. Equations (A2) and (A3) applied to (A1) cause $T_n(\omega'')$ to map to

$$\frac{G_A(\omega)}{C_B} = (-1)^n \cdot\cos\left[n\cos^{-1}\left(\frac{\sin^2(\pi\omega_a/2\omega_0) - 2\sin^2(\pi\omega/2\omega_0)}{\sin^2(\pi\omega_a/2\omega_0)}\right)\right] \tag{A4}$$

which is the function sketched in Fig. 9(c) for the case of $n = 4$. Here ω_a is a mapping of ω_a', and $\omega_0 - \omega_a = \omega_b - \omega_0$. In Section II of this paper n is replaced by $M/2$ where M is the number of zeros (all on the $j\omega$ axis) per period of the frequency response. In (A4) C_B on the left is an arbitrary scale factor which can be used to scale $G_A(\omega)$ in (3).

In Fig. 9(a)–(c) the equal-ripple regions all have ripple extremities of ± 1. As a result, $G_A(\omega_0)/C_B$ is equal to the ratio between the maximum passband signal obtained at ω_0 and the maximum stopband signal (which is here scaled to be one). Conversion of this ratio to decibels gives (1) where it should be noted that the $\cos^{-1}$ and cos in (A4) have become $\cosh^{-1}$ and cosh, respectively, since the argument of the $\cos^{-1}$ function is greater than one for $\omega_a < \omega < \omega_b$. The zeros of $G_A(\omega)$ occur at frequencies for which the square bracket in (A4) is equal to an odd multiple of $\pi/2$. Solving for these frequencies leads to (2).

APPENDIX B

DERIVATION OF THE EQUATIONS FOR THE TYPE 2 CASE

The equations in Section III were derived using a conformal mapping and the electrostatic potential analogy for transfer functions [3]–[5]. The reader is referred to the References for the details of this analogy. But, briefly, the general idea of the analogy is as follows. Suppose that we have a transfer function $G(p)$ defined in the complex-frequency plane $p = \sigma + j\omega$ by

$$G(p) = \frac{(p - p_1)(p - p_3)}{(p - p_2)(p - p_4)}. \tag{B1}$$

If we take the log of this we obtain

$$\begin{aligned}\ln G(p) &= \ln(p - p_1) + \ln(p - p_3) - \ln(p - p_2) \\ &\quad - \ln(p - p_4) \\ &= \ln|G(p)| + j\arg G(p).\end{aligned} \tag{B2}$$

This is mathematically identical to a two-dimensional complex potential due to infinite filaments of positive charge which are directed normal to the p plane and located at the poles p_2 and p_4, along with filaments of negative charge located at the zeros p_1 and p_3. The real part of the complex potential is the ordinary electrostatic potential while the imaginary part is the flux function. The reason for using this analogy in this work is because it can be shown [3] that if an infinite conducting plate is introduced normal to the p plane, and if the resulting flux lines about the plate are determined, by quantizing the charge on the plate at appropriate flux-line locations and removing the plate, an equal-ripple band will result in the region where the plate had been. Thus the electrostatic potential analogy is a useful tool for synthesizing transfer functions having equal-ripple bands.

The transfer function in Fig. 2(b) has periodic equal-ripple bands where the rows of zeros occur along the $j\omega$ axis. Using the potential analogy to achieve these equal-ripple bands, we would start out with filaments of negative charge at the off-$j\omega$-axis locations and conducting plates with distributed negative charge where equal-ripple bands are required. This problem is unnecessarily complex as it stands, and it can be simplified considerably by use of the mapping function (6). Using this mapping, the configuration in Fig. 10, which has an infinite periodic arrangement of charged plates in the p plane, maps to the arrangement in the p' plane of Fig. 11 which has a single charged plate.

Let us relate the synthesis of the transfer functions in Fig. 2(a) and (b) to the potential problems in Figs. 10 and 11, respectively. The transfer function in Fig. 2(b) has a total of eight zeros per period of which six are on the $j\omega$ axis and two zeros (or four half-zeros) are off of the $j\omega$ axis. These are matched by an equal number of poles at infinity. Accordingly, we will place six units of negative charge on each plate in Fig. 10, two units of negative

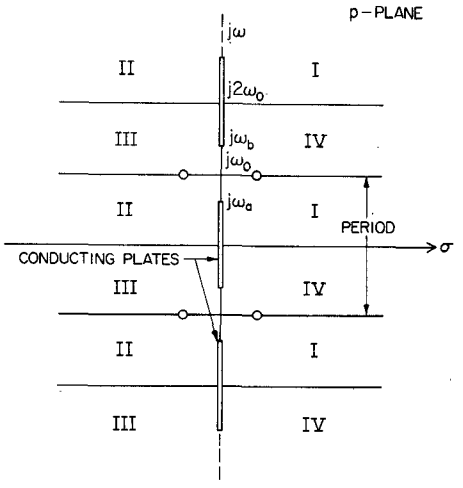

Fig. 10. Electrostatic problem for obtaining bandpass type 2 transfer functions.

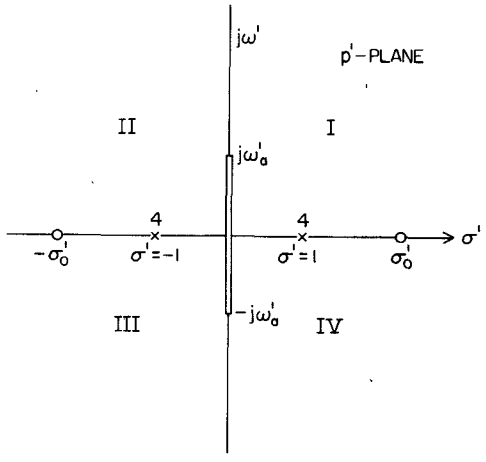

Fig. 11. High-pass equivalent for the problem in Fig. 10.

charge per period in filaments off of the $j\omega$ axis, and an equal amount of positive charge in filaments at infinity. The mapping (6) maps part of the point at infinity in the p plane to $\sigma' = \pm 1$ on each sheet of the p' plane. As a result, the eight units of positive charge at infinity per period in Fig. 10 are mapped to *two* four-unit filaments indicated by the crosses at $\sigma' = \pm 1$ in Fig. 11.

Tuttle [3, p. 922] has shown that the complex potential W about an arrangement of both quantized and distributed charge such as that in Fig. 11 can be calculated from

$$W = V + j\Phi = \ln | U | + j \arg U \qquad \text{(B3)}$$

where

$$U = \left[\frac{(p'^2 + \omega_a'^2)^{1/2} + m_0 p'}{(p'^2 + \omega_a'^2)^{1/2} - m_0 p'}\right]^{(M+2)/2} \cdot \left[\frac{(p'^2 + \omega_a'^2)^{1/2} - m_1 p'}{(p'^2 + \omega_a'^2)^{1/2} + m_1 p'}\right]. \qquad \text{(B4)}$$

Here V is the scalar potential function, Φ is the flux function, m_0 and m_1 are defined by (11), and M is the number (odd or even) of charges on the metal plate. The flux or phase function $\Phi = \arg U$ is obtained from (B4) and is given by the left side of (16).

Let us suppose that the poles and zeros in Fig. 2(a) are replaced by infinite filaments of positive and negative charge, respectively. The resulting potential will have equal ripple between $-\omega_a'$ and ω_a'. The charge configuration in Fig. 2(a) can be obtained from that in Fig. 11 by proper quantizing of the distributed charge on the metal plate [3]–[5]. For M even the charge should be quantized into unit filaments at the flux lines emanating from the right side of the plate which are odd multiples of $\pi/2$. If M is odd the charge should be quantized where integer multiples of π flux lines emerge from the plate. As mentioned previously, the left side of (16) is the flux function for the right side of the plate in Fig. 11 while the right side of (16) specifies the flux line where quantization is to take place. Solution of (16) locates where the $j\omega$-axis filaments (or zeros) should be in Fig. 2(a). By use of the mapping (6) in the form given in (18) and (19), the desired transfer function of the type in Fig. 2(b) is obtained.

The functions U in (B4) and U^2 are, respectively, e^W and e^{2W} where W is the complex potential defined in (B3). From [3, pp. 922–925] it can be seen that the complex potential $2W_q$ after charge quantization is accomplished is related to the potential $2W$ before charge quantization by

$$e^{2W_q} = \cosh (2W) \pm 1 \qquad \text{(B5)}$$

where the upper sign applies for M even and the lower sign for M odd. Substituting (B3) and (B4) in (B5) and expressing the ratio $e^{2W_q}(\omega')/e^{2W_q}(\omega_a')$ in decibels gives (9).

ACKNOWLEDGMENT

The authors wish to thank B. A. Hanson for his assistance in some of the computer programming involved in this work.

REFERENCES

[1] W. L. Weeks, *Antenna Engineering*. New York: McGraw-Hill, 1968, pp. 101–115.
[2] R. Bracewell, *The Fourier Transform and Its Applications*. New York: McGraw-Hill, 1965, ch. 3.
[3] D. F. Tuttle, Jr., *Network Synthesis*. New York: Wiley, 1958, ch. 14.
[4] G. L. Matthaei, "Filter transfer function synthesis," *Proc. IRE*, vol. 41, pp. 377–382, Mar. 1953.
[5] J. A. Miller, "The design of maximally flat and Chebyshev nonrecursive digital filters via the 'potential analogy,'" Ph.D. dissertation, Stanford Univ., Stanford, CA, 1971.
[6] F. G. Marshall, C. O. Newton, and E. G. S. Paige, "Surface acoustic wave multistrip components and their applications," *IEEE Trans. Microwave Theory Tech. (Special Issue on Microwave Acoustic Signal Processing)*, vol. MTT-21, pp. 216–225, Apr. 1973.
[7] R. H. Tancrell, "Improvement of an acoustic surface-wave filter with a multistrip coupler," *Electron. Lett.*, vol. 9, pp. 316–317, July 12, 1973.
[8] T. W. Bristol, "Synthesis of periodic unapodized surface wave transducers," in *1972 IEEE Ultrasonic Symp. Proc.* (New York), pp. 377–380.
[9] R. H. Tancrell, "Analytic design of surface wave bandpass filters," in *1972 IEEE Ultrasonic Symp. Proc.* (New York), pp. 215–217.
[10] R. H. Tancrell and M. G. Holland, "Acoustic surface wave filters," *Proc. IEEE*, vol. 59, pp. 393–409, Mar. 1971.

[11] G. L. Matthaei, D. Y. Wong, and B. P. O'Shaughnessy, "Simplifications for the analysis of interdigital surface-wave devices," *IEEE Trans. Sonics Ultrason.*, vol. SU-22, pp. 105–114, Mar. 1975.
[12] G. L. Matthaei and D. Y. Wong, "Some techniques for interdigital acoustic-surface-wave filter synthesis," in *1973 IEEE Ultrasonics Symp. Proc.* (New York), pp. 427–432.
[13] C. S. Hartmann and B. G. Secrest, "End effects in interdigital surface wave transducers," in *1972 IEEE Ultrasonic Symp. Proc.* (New York), pp. 413–416.
[14] W. R. Smith, Jr., "Circuit model analysis for interdigital transducers with arbitrary stripe-to-gap ratios, polarity sequences, and harmonic operation," in *1974 IEEE Ultrasonic Symp. Proc.* (New York), pp. 412–417.

Symmetrical Four-Port Edge-Guided Wave Circulators

PIETRO DE SANTIS, MEMBER, IEEE, AND FIORAVANTE PUCCI

Abstract—**Four-port microwave-integrated-circuit (MIC) edge-guided wave circulators (EGC) have been designed, fabricated, and tested. A mathematical characterization of the strip conductor's shape as well as a precise mechanical control of the bias inhomogeneity are provided. By means of these two techniques the reproducibility of the device is greatly improved with respect to that of the EGC obtained by the traditional cut-and-try methods.**

X-band performance data are presented and related to the spatial distribution of the effective magnetic permeability μ_{eff} in the ferrite substrate. Experimental evidence is reported that an efficient circulator action occurs when $\mu_{eff} < 0$ at some point under the central circular shield.

The spatial distribution of the RF electric field at the circulator's surface is investigated by a mechanical probing technique. It is found that in the lower part of the operation band, RF fields of considerable amplitude extend in the air in the region between the guiding edge and the substrate's edge.

I. INTRODUCTION

THE rigorous solution of a symmetrical four-port circulator by using the Green's function method [1] requires three circulation conditions to be simultaneously satisfied [2]. Each condition may be formulated in terms of an infinite series of modes and subsequently approximated by a summation over a finite number of terms.

In [2] it is demonstrated that even if a large number of modes are considered, only a few discrete frequencies exist at which perfect circulation is achieved. This result is at variance with that of a three-port circulator for which perfect circulation conditions may be met over a large frequency band [3]. Alternatively, it can be stated that a four-port junction circulator is inherently narrow band and no "continuous tracking principle" [3] can be found for it.

In light of these considerations, a study of the broadband performance of a four-port edge-guided wave circulator (EGC) [4] seems to be of particular interest. Furthermore, since no difference exists in the basic principles of operation of three-port and four-port EGC's, the experience on the former [5] could be usefully extended to the latter.

Another motivation of the present work is the fact that the results published so far on the subject [4] report on EGC's with a rather poor performance over a limited bandwidth.

In the following section a brief presentation is made of the physical principles which underlie the performance of EGC's. Subsequently, these results are applied to the design of four-port circulators. In Section IV an experimental investigation is presented on the nature of the volume-wave modes which resonate under conditions of positive effective magnetic permeability. In Section V the performance data of various types of four-port symmetrical EGC's are displayed and compared to the theoretical predictions. The paper is concluded by a study on the spatial distribution of the RF fields existing in a four-port EGC.

II. PRELIMINARY CONSIDERATIONS

In a previous work [5] the present authors reported on the construction of a three-port EGC. On that occasion a precise definition of EGC's was given in order to understand clearly how they differ from the traditional Y junction microwave-integrated-circuit (MIC) circulators.

Referring the reader to [5] for the details, here we simply recall that the distinguishing feature of an EGC is the presence of a transversal field displacement effect in the tapered sections of the device. This phenomenon is absent in a traditional MIC circulator because the impedance transformers are deposited on an isotropic substrate and is present here because the whole substrate is made of a ferrite magnetized perpendicular to the ground plane.

Manuscript received January 30, 1975; revised June 23, 1975.
The authors are with the Department of Research, Selenia S.p.A., Rome, Italy.